How to cite: *Angew. Chem. Int. Ed.* **2025**, *64*, e202508152
doi.org/10.1002/anie.202508152

Siloxane Electrolytes **Hot Paper**

Origin of Anion-Rich Solvation Structures in Siloxane Electrolytes

Yao-Peng Chen, Yi-Lin Niu, Zhao Zheng, Xiang Chen, Yu-Chen Gao, Nan Yao, Rui Zhang, and Qiang Zhang**

Abstract: High-voltage lithium (Li) metal batteries (LMBs) are promising next-generation high-energy-density rechargeable batteries. Siloxane electrolytes exhibit excellent performance in high-voltage LMBs. Herein, the mechanisms responsible for the Li metal compatibility and high-voltage resistance of siloxane electrolytes were probed by classical molecular dynamics (MD) simulations, first-principles calculations, and experimental characterizations. Siloxane electrolytes have been demonstrated to deliver anion-rich solvation structures, which are induced by weak Li ion (Li^+)–solvent interactions and strong Li^+–anion interactions. The silicon (Si)—oxygen (O) bond energy of siloxane is larger than that of carbon (C)—O of C-siloxane (replacing Si atoms in siloxane with C atoms) because the atomic radius of Si is larger than that of C, and the Pauli exclusion of Si is smaller than that of C. Additionally, ab initio molecular dynamics (AIMD) simulations revealed that the decomposition of siloxane produces substances containing Si—O fragments on Li metal surfaces, which is beneficial for interfacial stability. This work reveals the mechanism of interfacial stability and intrinsic stability of siloxane electrolytes, providing a theoretical basis for the practical application of siloxane electrolytes in high-voltage LMBs.

Introduction

Lithium-ion batteries (LIBs) have been widely applied in modern society, from portable electronic devices to electric vehicles.[1–5] However, the energy density of routine LIBs can hardly meet the growing demands from the above application scenarios. For instance, the energy density of both lithium nickel manganese cobalt oxide ($LiNi_xMn_yCo_{1-x-y}O_2$ (NMC))- and lithium iron phosphate ($LiFePO_4$)-based LIBs is generally below 300 Wh kg^{-1}.[6] In contrast, an energy density higher than 500 Wh kg^{-1} is usually required for low-altitude economy applications.[7,8] As a result, it is urgent to explore next-generation rechargeable batteries with ultrahigh-energy density.

In order to build a high-energy-density battery, Li metal has been considered the "holy grail" of anode materials due to its ultrahigh specific capacity (3860 mAh g^{-1}) and very low electrode potential (−3.04 V vs. the standard hydrogen electrode).[9,10] Besides anodes, high-voltage cathode materials, such as $LiNi_{0.8}Mn_{0.1}Co_{0.1}O_2$ (NMC811), $LiNi_{0.905}Mn_{0.035}Co_{0.06}O_2$, and lithium nickel manganese oxide ($LiNi_{0.5}Mn_{1.5}O_4$), are also beneficial to build high-energy-density batteries, especially for those with an energy density higher than 500 Wh kg^{-1}.[11–16] However, the application of Li metal anodes and high-voltage cathodes generally induces severe electrode-electrolyte interfacial (EEI) reactions, which accelerate battery degradation and even cause safety hazards.[17–20]

Electrolyte engineering has been widely considered an effective strategy for building a stable EEI for high-voltage LMBs. High-concentration electrolytes (HCEs) and local high-concentration electrolytes (LHCEs) have been especially focused on due to their high compatibility with Li metal anodes.[21–23] Specifically, anion-rich solvation structures, namely, more anions appear around Li^+ compared with solvents, are generally delivered in these two kinds of electrolytes. Anion-rich solvation structures are beneficial for producing inorganic components such as LiF, Li_2O, and Li_3N in both solid-electrolyte interphase (SEI) and cathode-electrolyte interphase (CEI).[24–29] Inorganic component-rich SEIs are compact and contribute to a high Li plating/stripping coulombic efficiency (CE). However, HCEs and LHCEs achieve anion-rich solvation structures by increasing the concentration of lithium salts or introducing diluents, which inevitably raises material costs in principle. In contrast, weakly solvating electrolytes (WSEs) emerge as a new electrolyte system to achieve anion-rich solvation structures by utilizing weakly solvating solvents.[30–34]

Among various weakly solvating solvents such as siloxanes,[35–37] ethers,[38] and fluorinated ethers,[39–41] siloxanes have been widely demonstrated with a high Li plating/stripping CE and a wide electrochemical window (Figure 1a). Furthermore, siloxanes possess a similar density to ethers (~0.8 g cm^{-3}), while fluorinated ethers typically exhibit a higher density (~1.3 g cm^{-3}). Siloxane electrolytes demonstrate comparable viscosity to LHCEs while offering lower costs than fluorinated ethers. The fluorine-free compo-

[*] Y.-P. Chen, Y.-L. Niu, Dr. Z. Zheng, Dr. X. Chen, Y.-C. Gao, N. Yao, Prof. Q. Zhang
Beijing Key Laboratory of Complex Solid State Batteries & Tsinghua Center for Green Chemical Engineering Electrification, Department of Chemical Engineering, Tsinghua University, Beijing 100084, China
E-mail: xiangchen@mail.tsinghua.edu.cn
zhang-qiang@mails.tsinghua.edu.cn
Dr. R. Zhang
Beijing Huairou Laboratory, Beijing 101400, China

Additional supporting information can be found online in the Supporting Information section

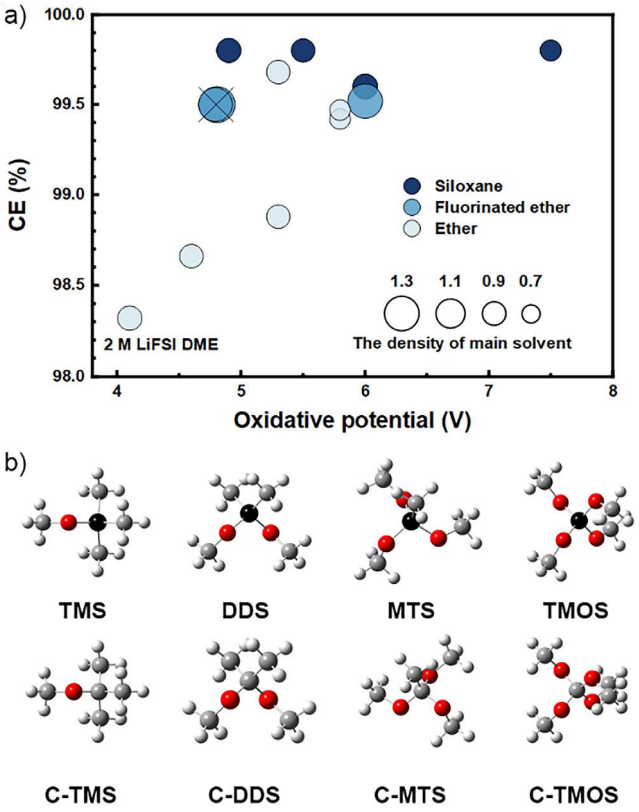

Figure 1. The electrochemical performance of siloxane electrolytes. a) CE, oxidation potential, and the density of solvents reported in the literature. Both CE and oxidation potential determine where the center of a bubble is located. The color and diameter of the bubbles represent the category and density of the solvents, respectively. A cross mark within a bubble indicates overlapping CE/oxidation potential coordinates. The four uncolored circles above the horizontal "density of main solvent" line provide a size reference for density values (labeled numerically). CE data were obtained from Li | Cu cells, and oxidation voltage data were measured using the linear sweep voltammetry (LSV) method. Data are extracted from Refs. [35–43]. b) The optimized geometrical structures of solvent molecules. White, grey, red, and black balls represent H, C, O, and Si, respectively.

sition presents clear environmental and economic advantages over fluorinated diluents.[42] This combination of exceptional electrochemical performance and favorable physicochemical properties establishes siloxane electrolytes as highly promising candidates for high-voltage LMB electrolytes. For example, Huang et al.[42] reported a series of siloxane solvent molecules, such as tetraethyl orthosilicate, methyltriethoxysilane, dimethyldiethoxysilane, and dimethyldimethoxysilane (DMMS). These siloxane-based electrolytes with lithium bis(fluorosulfonyl)imide (LiFSI) as the salt delivered a high Li plating/stripping CE larger than 99%. In particular, 1.5 M LiFSI DMMS achieved a CE of 99.8% and an oxidation voltage of 4.9 V. The assembled 4.5 V $LiCoO_2$||Li cells retained 95% capacity after 200 cycles, and 1.4 Ah NCM811||Li pouch cells with 2.5 g Ah^{-1} lean electrolyte achieved 96% capacity retention after 140 cycles. The promising electrochemical performances of siloxane electrolytes were usually explained by their anion-rich solvation structures and intrinsic stability. However, the fundamental mechanisms of siloxane on such characteristics have not been well explored. Probing the siloxane effects can facilitate the molecular-level design of siloxane electrolytes and promote the practical application of high-voltage LMBs.

In this contribution, the origin of anion-rich solvation structures and stability in siloxane electrolytes was probed by combining multiscale simulations and experimental characterizations. Four siloxanes (trimethylmethoxysilane (TMS), dimethoxydimethylsilane (DDS), methyltrimethoxysilane (MTS), and tetramethyl orthosilicate (TMOS)) electrolytes and four corresponding ether (methyl *tert*-butyl ether (C-TMS), 2,2-dimethoxypropane (C-DDS), trimethyl orthoacetate (C-MTS), and tetramethoxymethane (C-TMOS)) electrolytes were systematically investigated (Figure 1b), including their geometrical structures, electronic structures, interaction with a Li^+, and solvation structures. The anion-rich solvation structures of siloxanes were ascribed to the relative binding energies between Li^+–solvent and Li^+–anion. The high intrinsic stability of siloxane is explained by the higher bond energy of Si—O compared with C—O bond due to the larger radius and smaller Pauli repulsion of Si compared with C. AIMD simulations were further conducted to probe the interfacial reaction mechanism between siloxane electrolytes and Li metal anodes. Decomposition substances containing Si—O fragments were confirmed, which is supposed to enhance EEI stability and is consistent with experiments. This work reveals the siloxane effects on electrolyte solvation structures and molecular stability, facilitating the rational design of advanced electrolytes and the application of siloxane electrolytes to next-generation high-energy-density rechargeable batteries.

Results and Discussion

Anion-Rich Solvation Structures

Siloxanes (TMS, DDS, MTS, and TMOS) and ethers (C-TMS, C-DDS, C-MTS, C-TMOS, and 1,2-dimethoxyethane (DME)) were focused on (Figure 1) in this contribution. The four siloxanes were chosen because they have been demonstrated to exhibit excellent electrochemical performance, including high Li plating/stripping CE and oxidation potential (Figure 1a). By replacing Si atoms in the siloxane structure with C atoms (Figure 1b), these C-siloxane (C-TMS, C-DDS, C-MTS, and C-TMOS) molecules afford a direct comparison and further help to unveil the mysterious role of Si atoms on electrolyte solvation behaviors as well as functions. Additionally, DME was included as a reference solvent, as it is widely employed in LMBs due to its high Li plating/stripping CE.[43]

MD simulations were adopted to explore the solvation structures of electrolytes containing the above solvents and 1.0 M LiFSI (Figures 2a,b, S1, and Table S1). As a result, the FSI^- anions are uniformly distributed in typical strong electrolytes, i.e., DME. However, anions tend to produce clusters in siloxane electrolytes, which is a typical characteristic of WSEs. According to the radial distribution function (RDF)

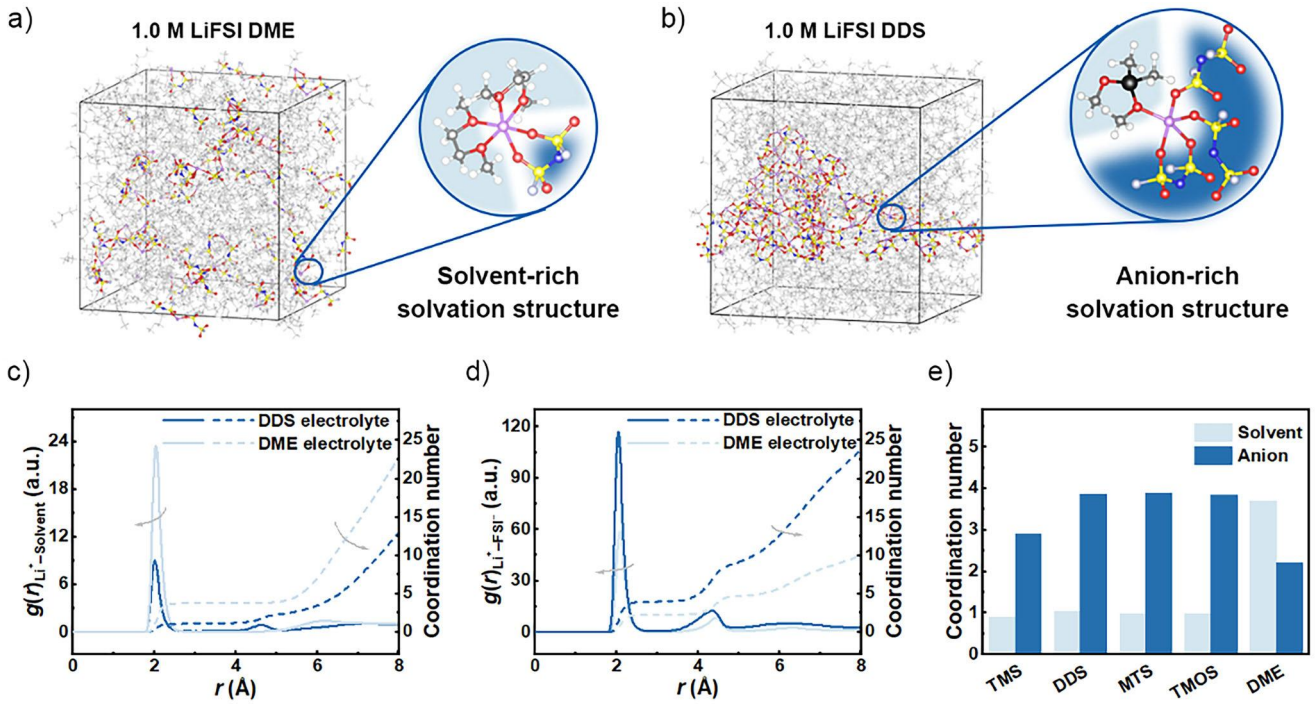

Figure 2. The anion-rich solvation structures of siloxane electrolytes. a) and b) MD snapshots and typical solvation structures. White, purple, grey, blue, red, cyan, black, and yellow balls represent H, Li, C, N, O, F, Si, and S, respectively. The radial distribution function ($g(r)$) and coordination number of c) Li^+–solvent and d) Li^+–FSI^-. e) The coordination number of 1.0 M LiFSI in various solvents.

analyses, Li^+ mainly interacts with O atoms in solvents and anions (Figures 2c,d and S2). Specifically, the peaks of Li^+–solvent (2.01 Å) and Li^+–FSI^- (2.03 Å) appear at nearly the same position in all electrolytes. In siloxane and C-siloxane electrolytes, the coordination number (CN) of solvents is smaller than that of anions (Table S2). Specifically, siloxane electrolytes render solvent and anion CN of 0.89 and 2.90 for TMS, 1.04 and 3.85 for DDS, 0.98 and 3.87 for TMS, and 0.97 and 3.84 for TMOS, respectively. Similarly, C-siloxane electrolytes exhibit solvent and anion CN of 0.94 and 3.80 for C-TMS, 0.89 and 3.88 for C-DDS, 1.07 and 3.87 for C-MTS, and 1.21 and 3.85 for C-TMOS, respectively. In contrast, the CN of the solvent (3.69) is substantially larger than that of the anion (2.19) in the DME electrolyte (Figure 2e). The WSE-featured phenomenon can be attributed to the structural characteristics of siloxane. The Si atoms have a significantly larger atomic radius (1.17 Å) compared with the C atom (0.77 Å). Additionally, Si atoms in siloxanes are typically surrounded by bulky functional groups, creating substantial steric hindrance around the O atoms. The increased steric hindrance in siloxanes restricts the accessibility of Li^+ to the solvent O atoms, thereby reducing the coordination ability of solvent with Li^+.

Raman spectra were further conducted to validate the MD simulation results (Figure 3a). Based on the number of Li^+ coordinated with an FSI^-, the solvation structures were classified into free FSI^- (no Li^+ coordinated with an FSI^-), contact ion pairs (CIPs, one Li^+ coordinated with an FSI^-), aggregate (AGG)-I (Two Li^+ coordinated with an FSI^-), and AGG-II (three Li^+ coordinated with an FSI^-). The Raman

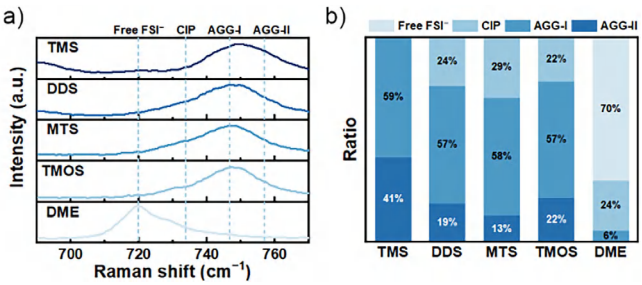

Figure 3. Experimental verification. a) Raman spectra of 1.0 M LiFSI in various solvents. b) The ratios of free FSI^-, CIP, AGG-I, and AGG-II in various electrolytes, as derived from Raman spectra.

shift of FSI^- in the range of 700–800 cm^{-1} is attributed to the S─N─S symmetric stretching vibration mode, which can be classified into four types, including free FSI^- (720 cm^{-1}), CIPs (733 cm^{-1}), AGG-I (747 cm^{-1}), and AGG-II (757 cm^{-1}). Peak deconvolution of the Raman spectra revealed distinct solvation structure distributions across different electrolytes (Figure 3b). In siloxane electrolytes, AGG-I was consistently the predominant species, accounting for 57%–59% of solvation structures. Specifically, TMS exhibited the highest degree of AGG with AGG-I (59%) and AGG-II (41%) as the only observed species. DDS showed a distribution of CIPs (24%), AGG-I (57%), and AGG-II (19%). Similarly, MTS displayed CIPs (29%), AGG-I (58%), and AGG-II (13%), while TMOS exhibited CIPs (22%), AGG-I (57%), and AGG-II (22%). In stark contrast, the DME electrolyte

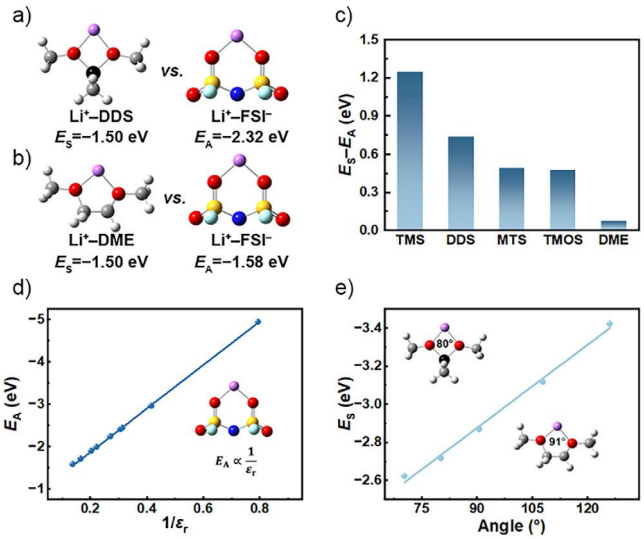

Figure 4. The origin of anion-rich solvation structures. The optimized geometrical structures of a) Li^+–DDS and Li^+–FSI^-, and b) Li^+–DME and Li^+–FSI^- in a solvation environment. White, purple, grey, blue, red, cyan, black, and yellow balls represent H, Li, C, N, O, F, Si, and S. E_S and E_A refer to Li^+–solvent and Li^+–anion binding energies, respectively. c) The relative binding energy between Li^+–solvent and Li^+–FSI^-. d) The correlation between Li^+–FSI^- binding energy and $1/\varepsilon_r$. e) The correlation between Li^+–solvent binding energy and O–Li^+–O angle in vacuum.

demonstrated significantly less aggregation, with free FSI^- as the dominant species (70%), followed by CIPs (24%) and minimal AGG-I (6%). These quantitative results further confirm that siloxane electrolytes promote AGG, with AGG-I as the primary solvation structure, whereas the DME electrolyte favors free FSI^- formation. The Raman results are consistent with the above MD simulation results.

Origin of Anion-Rich Solvation Structures

Solvation structures originate from the competitive coordination of solvent and anion with Li^+. Anion-rich solvation structures are preferentially formed when Li^+–solvent interaction is much weaker than Li^+–anion interaction. The binding energy quantitatively reflects the strength of the interaction among the solvent, anion, and Li^+. According to the density functional theory (DFT) calculation results (Figures 4a,b, S3, and S4), the binding energy of Li^+–siloxane is smaller than that of Li^+–DME (E_S values of −1.16 to −1.50 eV for siloxanes compared with −1.50 eV for DME), indicating the WSE characteristic of siloxane electrolytes. Furthermore, the binding energy of Li^+–siloxane is even lower than that of Li^+–C-siloxane (except for Li^+–TMS and Li^+–C-TMS, where E_S values are −1.16 and −1.09 eV, respectively), suggesting that the introduction of Si atoms can reduce the binding energy of the Li^+–solvent complex. In order to consider a quantitative description of WSEs, a descriptor of E_S-E_A was proposed. For siloxane electrolytes, E_S-E_A values range from 0.47 (TMOS) to 1.24 eV (TMS) (Figures 4c and S5), while C-siloxane electrolytes exhibit even higher values between 0.80 (C-MTS) and 2.69 eV (C-DDS) (Figures S6 and S7). These substantially positive values favor the formation of anion-rich solvation structures. In contrast, for the DME electrolyte, E_S-E_A is 0.08 eV, leading to the formation of solvent-rich solvation structures. More importantly, the E_S-E_A delivers a positive correlation with the ratio of AGG from Raman spectra, where TMS with the highest E_S-E_A value (1.24 eV) among siloxanes exhibits the highest degree of AGG (100% AGG structures), while DME with the lowest E_S-E_A value (0.08 eV) shows minimal AGG (only 6% AGG-I structures) (Figure S8).

To understand the origin of the WSE nature of siloxane electrolytes, the principles of Si atoms in regulating the binding energy were investigated. Intuitively, possible factors affecting the binding energy include the dielectric constant, dipole moment, bond length, charge, and bond angle (Figures S9–S13). The electrostatic interaction between Li^+ and FSI^- is influenced by the dielectric constant of the solution environment. As the dielectric constant of the solvent increases, the binding energy between Li^+ and FSI^- decreases.[44] Specifically, the binding energy of Li^+–FSI^- shows a significant positive correlation with the reciprocal of dielectric constant (Figure 4d). Siloxanes have a lower dielectric constant than DME, which results in larger binding energy between Li^+ and FSI^- in siloxane electrolytes compared to that in DME electrolytes (Figure S9). The dipole moment is related to the configuration of the solvent molecule, with symmetrical solvent molecules having low dipole moments.[45] However, there is no direct correlation between the dipole moment and the binding energy (Figure S10). The Li—O bond length also affects the Li^+–solvent binding energy. A longer Li—O bond length leads to a lower binding energy (Figure S14). Under the same coordination conditions, the Li—O bond length in siloxane is longer than in DME (Figure S11), resulting in a lower binding energy. The charge on O in siloxanes is higher than that on O in ethers (Figure S12), but this does not significantly affect Li^+–solvent binding energy. The effect of the O—Li—O bond angle on the binding energy was also considered. When Li^+ and the solvent form a chelate, a larger O—Li—O bond angle results in a larger Li^+–solvent binding energy (Figure 4e). The atomic radius of Si is larger than that of C, and the Si—O (or Si—C) bond length is also longer than that of C—O (C—C). When the atoms on the chelate ring are the identical, the O—Li—O bond angle in Li^+–siloxane is larger than that in Li^+–ether (Figure S13).

Collectively, the above findings clarify the fundamental role of Si atoms in establishing the WSE nature of siloxane electrolytes. The presence of Si, with its larger atomic radius (compared to C atoms) and distinct electronic properties, influences multiple parameters that contribute to the WSE nature. First, the larger Si atoms create more extended molecular geometries with longer bond lengths, resulting in increased Li—O bond length and thus weakened Li^+–solvent interactions. Furthermore, the incorporation of Si atoms leads to lower dielectric constants in siloxane solvents, strengthening Li^+–anion interactions relative to Li^+–solvent interactions. Additionally, the chelate structures formed between Li^+ and siloxanes create four-membered rings, whereas Li^+–DME complexes form five-membered rings.

Consequently, the O—Li—O bond angles in siloxane chelates are smaller than those in DME chelates, which further contributes to reduced Li^+–solvent binding energy in siloxane systems. This multifaceted influence of Si atoms on molecular geometry and physicochemical properties ultimately engineers an electrolyte environment where Li^+ preferentially associates with anions rather than only solvent molecules.

Thermodynamic Analysis of Solvent Stability

The thermodynamic stability of siloxane and C-siloxane was further investigated through DFT calculations, with HOMO and LUMO energy levels adopted as descriptors (Figures S15 and S16). The introduction of a Si atoms into molecules reduces both LUMO and HOMO energy levels, indicating reduced reductive stability and enhanced oxidative stability, respectively (Figures S17 and S18). Moreover, the interaction between Li^+ and solvents leads to a reduction in both LUMO and HOMO energy levels. The changes in LUMO and HOMO energy levels are related to the binding energy of the Li^+–solvent complex (Figures S19 and S20), which is consistent with previous reports.[46] When chelates are formed, the higher the binding energy between Li^+ and the solvent, the larger the changes in the LUMO and HOMO energy levels (Figures S21 and S22).

Bond energy can also reflect the stability of siloxane and C-siloxane. The bond energies of Si—C, Si—O, and O—C in siloxane and C—C, C—O, and O—C in C-siloxane were calculated. Both TMOS and C-TMOS have four —OCH_3 functional groups, and lack Si—C and C—C bonds. The bond energy analysis for DDS and C-DDS (Figure 5a) shows that in siloxane (DDS), the Si—O bond has the highest bond energy (−4.98 eV), followed by Si—C (−4.43 eV) and O—C (−4.35 eV). In contrast, in C-siloxane (C-DDS), the C—C bond exhibits the highest bond energy (−4.48 eV), followed by O—C (−3.97 eV) and C—O (−3.97 eV). A similar trend (Figure S23) was observed in other siloxane molecules (TMS, MTS, and TMOS) and their C-siloxane counterparts (C-TMS, C-MTS, and C-TMOS). The Si—O bond consistently exhibits the highest bond energy in siloxane, while the C—C bond is the strongest in C-siloxane. These results demonstrate that Si—C and O—C bonds are more susceptible to breaking in siloxane, whereas C—O and O—C bonds are more prone to breaking in C-siloxane. The bond strength further indicates that siloxane is more stable than C-siloxane. Notably, the bond energy of Si—O in siloxane (−4.83 to −5.14 eV) is significantly larger than that of C—O in C-siloxane (−3.86 to −4.17 eV), suggesting better stability of siloxane compared with C-siloxane. LSV tests further confirm the enhanced oxidative stability of siloxane compared to ether-based electrolytes, consistent with their bond energy differences.[47]

Bond energy decomposition further explores the effect of the introduction of Si atoms on bond energy. The total bond energy can be decomposed into four components,[48] namely E_{xrep}, E_{orb}, E_{els}, and E_c (Figure 5b). E_{xrep} represents the sum of E_x and E_{rep}, E_{orb} accounts for the energy contribution from interfragment electron transfer, E_{els} describes the classical electrostatic interaction between fragments, and E_c denotes

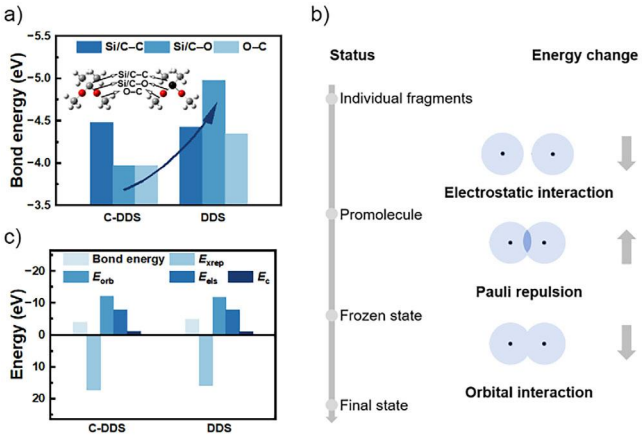

Figure 5. Bond energy analysis. a) Bond energy of solvent molecules. b) The bonding process involves multiple energy contributions. From individual fragments to the promolecule, classical electrostatic energy (E_{els}) dominates, complemented by exchange energy (E_x), DFT correlation energy (E_{DFTc}), and dispersion correction energy (E_{dc}). From the promolecule to the frozen state, Pauli repulsion energy (E_{rep}) becomes predominant. From the frozen state to the final state, orbital interaction energy (E_{orb}) facilitates further energy reduction, completing bond formation. Note that E_x and E_{rep} combine to form exchange-repulsion energy (E_{xrep}), while E_{DFTc} and E_{dc} constitute the Coulomb correlation energy (E_c). c) Si/C—O bond energy decomposition.

the Coulomb correlation effect on interfragment interactions. For DDS and C-DDS, the bond energy decomposition results reveal distinct contributions from each energy component (Figure 5c). The analysis shows that E_{xrep} in DDS (15.84 eV) is notably lower than that in C-DDS (17.22 eV), indicating that siloxane experiences weaker Pauli repulsion. While E_{orb} is comparable between the two systems (−11.87 eV vs. −12.15 eV), and E_{els} remain nearly identical (−7.94 eV vs. −7.90 eV), the reduced repulsion in DDS is the primary factor contributing to its stronger overall bond energy (−4.94 eV vs. −3.94 eV). The difference in E_{xrep} can be attributed to the larger atomic radius of Si compared to C, reducing steric hindrance and facilitating stronger Si—O bond energy formation. A similar trend (Figure S24) is observed for the other siloxanes (TMS, MTS, and TMOS) and C-siloxanes (C-TMS, C-MTS, and C-TMOS) molecules. These results collectively demonstrate that the introduction of Si atoms significantly reduces exchange-repulsion energy due to the large atomic radius of Si, which minimizes steric hindrance and enhances the stability of Si—O bonds. The bond energy decomposition results further support the conclusion that siloxane exhibits greater stability than C-siloxane.

Kinetic Analysis of Solvent Decomposition

AIMD simulations were further conducted to explore the decomposition mechanism of siloxane solvents on Li surface. DDS was specifically selected for the investigation because it demonstrated the most promising electrochemical performances in previous reports.[42,49–51] An interfacial model consisting of Li(110) surface and 10 DDS solvents was built

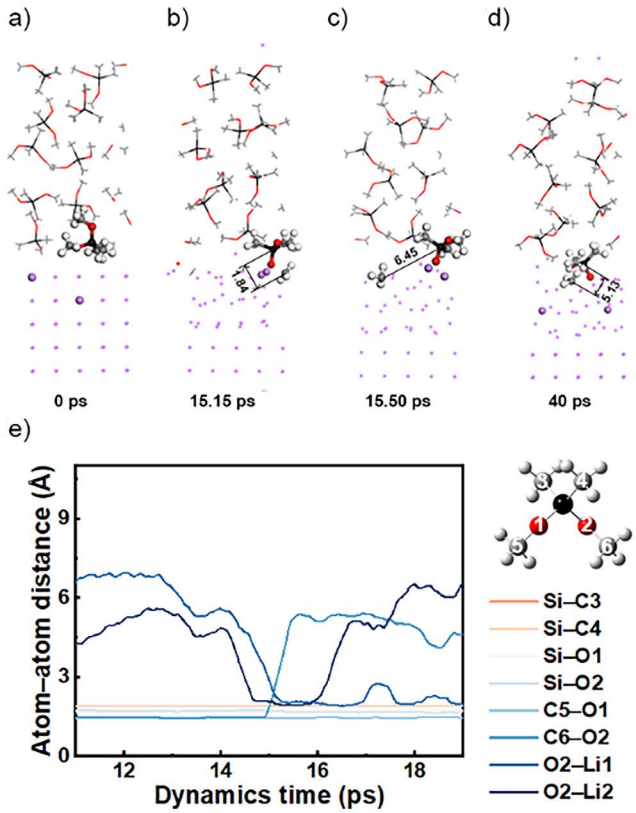

Figure 6. AIMD simulations of the decomposition of DDS on Li(110) surface. a)–d) Complete sequence of DDS molecule decomposition (unit: Å). e) Time evolution of DDS molecule decomposition between 10 and 20 ps.

and then simulated for 40 ps. According to the complete decomposition sequence (Figure 6a–d), a DDS molecule near the Li surface decomposed to produce CH_3 and $SiO(CH_3)_2(OCH_3)$. The theoretical calculation is consistent with previous experimental XPS results, which demonstrated the presence of O—Si—O and $Si(CH_3)_x$ fragments on the Li metal surface in siloxane-based electrolytes.[42] Specifically, the O2 atom of DDS molecule is approaching Li1 and Li2 atoms from 14 to 15 ps (Figure 6e). Then, C6—O2 bond length increased and finally broke at 15 ps. No other bond breaking was observed during the following simulations within 40 ps (Figure S25).

The AIMD simulation results reveal several important mechanistic insights. The observed decomposition process initiates with the interaction between Li atoms and the O atom of DDS, leading to the subsequent breaking of the C—O bond. This C—O bond-breaking mechanism can be attributed to the strong electron-donating effect of Li atoms, which significantly weakens the adjacent C—O. Notably, the Li—O interaction selectively induces C—O bond-breaking while preserving the Si—O bond throughout the simulation. The selective bond-breaking is consistent with the bond energy results that C—O bonds are more susceptible to breaking compared with Si—O bonds. The preservation of Si—O fragments in the decomposition products, as confirmed by experimental XPS results showing the presence of O—Si—O fragments, is particularly significant as it contributes to the formation of a stable SEI layer.[42] These findings not only elucidate the decomposition mechanism of DDS but also afford valuable insights for understanding other siloxane-based electrolytes, as many siloxanes share similar structural units with DDS.

Conclusions

The origin of anion-rich solvation structures and solvent stability in siloxane electrolytes was comprehensively investigated by combining multiscale simulations and experimental characterizations. The anion-rich solvation structure in siloxane electrolytes was confirmed by both MD simulations and NMR characterizations. An energy descriptor of $E_S - E_A$ was proposed to explain the WSE characteristics of siloxane electrolytes. The intrinsic stability of siloxane solvents was further confirmed by frontier molecular orbital and bond energy decomposition analyses that the bond energy in siloxanes follows the order of Si—O > Si—C ≈ O—C. Last but not least, AIMD simulations validated the stability of siloxane solvents in that no Si bond was broken during 40 ps simulations. Previous studies have reported that anion-rich solvation structures of siloxane electrolytes can promote the formation of inorganic interface films, which are crucial for the performance of high-voltage LMBs. This work elucidates the fundamental role of Si atoms in regulating anion-rich solvation structures in siloxane electrolytes and highlights the superior stability of siloxane molecules. These insights offer a molecular-level understanding of the design principles governing siloxane electrolytes for high-voltage lithium metal batteries, paving the way for their practical implementation in next-generation rechargeable batteries.

Acknowledgements

This work was supported by the National Key Research and Development Program (2021YFB2500300), the Beijing Municipal Natural Science Foundation (L247015 and L233004), the National Natural Science Foundation of China (T2322015, 92472101, 22393903, 22393900, and 52394170), the S&T Program of Hebei (22344402D), the Xplorer Prize, and the Tsinghua University Initiative Scientific Research Program. The authors acknowledged the support from Tsinghua National Laboratory for Information Science and Technology for theoretical.

Conflict of Interests

The authors declare no conflict of interest.

Data Availability Statement

The data that support the findings of this study are available from the corresponding author upon reasonable request.

Keywords: Anion-rich solvation structures · Lithium batteries · Molecular simulations · Siloxane electrolytes · Solid electrolyte interphase

[1] K. Xu, *Chem. Rev.* **2014**, *114*, 11503–11618.
[2] M. Winter, B. Barnett, K. Xu, *Chem. Rev.* **2018**, *118*, 11433–11456.
[3] R. Schmuch, R. Wagner, G. Hörpel, T. Placke, M. Winter, *Nat. Energy* **2018**, *3*, 267–278.
[4] Z. Zhu, T. Jiang, M. Ali, Y. Meng, Y. Jin, Y. Cui, W. Chen, *Chem. Rev.* **2022**, *122*, 16610–16751.
[5] X. Zeng, M. Li, D. A. El-Hady, W. Alshitari, A. S. Al-Bogami, J. Lu, K. Amine, *Adv. Energy Mater.* **2019**, *9*, 1900161.
[6] Y. Wu, L. Xie, H. Ming, Y. Guo, J.-Y. Hwang, W. Wang, X. He, L. Wang, H. N. Alshareef, Y.-K. Sun, J. Ming, *ACS Energy Lett.* **2020**, *5*, 807–816.
[7] H. Du, X. Zhang, H. Yu, *eTransportation* **2025**, *23*, 100382.
[8] V. Viswanathan, A. H. Epstein, Y.-M. Chiang, E. Takeuchi, M. Bradley, J. Langford, M. Winter, *Nature* **2022**, *601*, 519–525.
[9] X.-B. Cheng, R. Zhang, C.-Z. Zhao, Q. Zhang, *Chem. Rev.* **2017**, *117*, 10403–10473.
[10] D. Lin, Y. Liu, Y. Cui, *Nat. Nanotechnol.* **2017**, *12*, 194–206.
[11] Y. Jie, S. Wang, S. Weng, Y. Liu, M. Yang, C. Tang, X. Li, Z. Zhang, Y. Zhang, Y. Chen, F. Huang, Y. Xu, W. Li, Y. Guo, Z. He, X. Ren, Y. Lu, K. Yang, S. Cao, H. Lin, R. Cao, P. Yan, T. Cheng, X. Wang, S. Jiao, D. Xu, *Nat. Energy* **2024**, *9*, 987–998.
[12] R. Qiao, Y. Zhao, S. Zhou, H. Zhang, F. Liu, T. Zhou, B. Sun, H. Fan, C. Li, Y. Zhang, F. Liu, X. Ding, J. W. Choi, A. Coskun, J. Song, *Chem* **2025**, *11*, 102306.
[13] S. Zhang, R. Li, T. Deng, Q. Ma, X. Hong, H. Zhang, R. Zhang, S. Ding, Y. Wu, H. Zhu, M. Li, H. Zhang, D. Lu, B. Ma, L. Lv, Y. Li, L. Chen, Y. Shen, R. Guo, X. Fan, *Nat. Energy* **2024**, *9*, 1285–1296.
[14] T. Tang, C. Sun, Y. Li, M. Tong, J. Lu, C. Lai, *Angew. Chem. Int. Ed.* **2025**, *64*, e202417471.
[15] H. Zhang, Z. Zeng, S. Cheng, J. Xie, *eScience* **2024**, *4*, 100265.
[16] X. Zhou, F. Hong, S. Wang, T. Zhao, J. Peng, B. Zhang, W. Fan, W. Xing, M. Zuo, P. Zhang, Y. Zhou, G. Lv, Y. Zhong, W. Hua, W. Xiang, *eScience* **2024**, *4*, 100276.
[17] X. Fan, C. Wang, *Chem. Soc. Rev.* **2021**, *50*, 10486–10566.
[18] J. Xiang, Y. Wei, Y. Zhong, Y. Yang, H. Cheng, L. Yuan, H. Xu, Y. Huang, *Adv. Mater.* **2022**, *34*, 2200912.
[19] Y. Chen, Z. Ma, Y. Wang, P. Kumar, F. Zhao, T. Cai, Z. Cao, L. Cavallo, H. Cheng, Q. Li, J. Ming, *Energy Environ. Sci.* **2024**, *17*, 5613–5626.
[20] X. Chen, Q. Zhang, *Acc. Chem. Res.* **2020**, *53*, 1992–2002.
[21] G. A. Giffin, *Nat. Commun.* **2022**, *13*, 5250.
[22] H. Wang, Z. Yu, X. Kong, S. C. Kim, D. T. Boyle, J. Qin, Z. Bao, Y. Cui, *Joule* **2022**, *6*, 588–616.
[23] Z. Zhao, A. Wang, A. Chen, Y. Zhao, Z. Hu, K. Wu, J. Luo, *Angew. Chem. Int. Ed.* **2024**, *63*, e202412239.
[24] P. Xiao, X. Yun, Y. Chen, X. Guo, P. Gao, G. Zhou, C. Zheng, *Chem. Soc. Rev.* **2023**, *52*, 5255–5316.
[25] Y. S. Meng, V. Srinivasan, K. Xu, *Science* **2022**, *378*, eabq3750.
[26] J. Chen, Y. Zhang, H. Lu, J. Ding, X. Wang, Y. Huang, H. Ma, J. Wang, *eScience* **2023**, *3*, 100135.
[27] X. Min, L. Wang, Y. Wu, Z. Zhang, H. Xu, X. He, *J. Energy Chem.* **2025**, *106*, 63–70.
[28] S.-Y. Sun, X.-Q. Zhang, X.-Y. Yan, Z. Zheng, Q.-K. Zhang, J.-Q. Huang, *EES Batteries* **2025**, *1*, 340–363.
[29] H. Wang, H. Wang, *EES Batteries* **2025**, *1*, 217–226.
[30] Y. X. Yao, X. Chen, C. Yan, X. Q. Zhang, W. L. Cai, J. Q. Huang, Q. Zhang, *Angew. Chem. Int. Ed.* **2021**, *60*, 4090–4097.
[31] H. Ma, Q. Wang, H. Lu, Y. Si, X. Kong, J. Wang, *Chem. Eng. J.* **2024**, *479*, 147557.
[32] Y.-X. Yao, L. Xu, C. Yan, Q. Zhang, *EES Batteries* **2025**, *1*, 9–22.
[33] R. Xu, A. Hu, Z. Wang, K. Chen, J. Chen, W. Xu, G. Wu, F. Li, J. Wang, J. Long, *J. Energy Chem.* **2025**, *105*, 35–43.
[34] Y. Wang, Y. Li, C. Li, Y. Guo, L. Yu, X. Li, T. Li, *J. Energy Chem.* **2025**, *106*, 681–687.
[35] B. Ma, H. Zhang, R. Li, S. Zhang, L. Chen, T. Zhou, J. Wang, R. Zhang, S. Ding, X. Xiao, T. Deng, L. Chen, X. Fan, *Nat. Chem.* **2024**, *16*, 1427–1435.
[36] H. Zhang, R. Li, L. Chen, Y. Fan, H. Zhang, R. Zhang, L. Zheng, J. Zhang, S. Ding, Y. Wu, B. Ma, S. Zhang, T. Deng, L. Chen, Y. Shen, X. Fan, *Angew. Chem. Int. Ed.* **2023**, *62*, e202218970.
[37] Y. Wang, Y. Ni, S. Xu, Y. Lu, L. Shang, Z. Yang, K. Zhang, Z. Yan, W. Xie, J. Chen, *J. Am. Chem. Soc.* **2025**, *147*, 10772–10783.
[38] Z. Li, H. Rao, R. Atwi, B. M. Sivakumar, B. Gwalani, S. Gray, K. S. Han, T. A. Everett, T. A. Ajantiwalay, V. Murugesan, N. N. Rajput, V. G. Pol, *Nat. Commun.* **2023**, *14*, 868.
[39] Z. Yu, H. Wang, X. Kong, W. Huang, Y. Tsao, D. G. Mackanic, K. Wang, X. Wang, W. Huang, S. Choudhury, Y. Zheng, C. V. Amanchukwu, S. T. Hung, Y. Ma, E. G. Lomeli, J. Qin, Y. Cui, Z. Bao, *Nat. Energy* **2020**, *5*, 526–533.
[40] Z. Yu, P. E. Rudnicki, Z. Zhang, Z. Huang, H. Celik, S. T. Oyakhire, Y. Chen, X. Kong, S. C. Kim, X. Xiao, H. Wang, Y. Zheng, G. A. Kamat, M. S. Kim, S. F. Bent, J. Qin, Y. Cui, Z. Bao, *Nat. Energy* **2022**, *7*, 94–106.
[41] I. R. Choi, Y. Chen, A. Shah, J. Florian, C. Serrao, J. Holoubek, H. Lyu, E. Zhang, J. H. Lee, Y. Lin, S. C. Kim, H. Park, P. Zhang, J. Lee, J. Qin, Y. Cui, Z. Bao, *Nat. Energy* **2025**, *10*, 365–379.
[42] Y. Huang, R. Li, S. Weng, H. Zhang, C. Zhu, D. Lu, C. Sun, X. Huang, T. Deng, L. Fan, L. Chen, X. Wang, X. Fan, *Energy Environ. Sci.* **2022**, *15*, 4349–4361.
[43] A.-M. Li, O. Borodin, T. P. Pollard, W. Zhang, N. Zhang, S. Tan, F. Chen, C. Jayawardana, B. L. Lucht, E. Hu, X.-Q. Yang, C. Wang, *Nat. Chem.* **2024**, *16*, 922–929.
[44] X. Chen, X. Q. Zhang, H. R. Li, Q. Zhang, *Batteries Supercaps* **2019**, *2*, 128–131.
[45] Y.-C. Gao, N. Yao, X. Chen, L. Yu, R. Zhang, Q. Zhang, *J. Am. Chem. Soc.* **2023**, *145*, 23764–23770.
[46] X. Chen, H.-R. Li, X. Shen, Q. Zhang, *Angew. Chem. Int. Ed.* **2018**, *57*, 16643–16647.
[47] Y. Yang, J. Lu, W. Ni, D. Peng, W. Chen, Y. Fu, J. Wang, *Adv. Funct. Mater.* **2025**, *35*, 2508056.
[48] T. Lu, Q. Chen, *J. Phys. Chem. A* **2023**, *127*, 7023–7035.
[49] M. Li, H. Chen, Y. Wang, X. Chen, J. Wu, J. Su, M. Wang, X. Li, C. Li, L. Ma, X. Li, Y. Chen, *J. Mater. Chem. A* **2023**, *11*, 11721–11729.
[50] Y. Wang, J. Liu, H. Ji, S. Wang, M. Wang, X. Zhou, T. Qian, Y. Zheng, C. Yan, *Adv. Mater.* **2025**, *37*, 2412155.
[51] X. Yin, B. Li, H. Liu, B. Wen, J. Liu, M. Bai, Y. Zhang, Y. Zhao, X. Cui, Y. Su, G. Gao, S. Ding, W. Yu, *Joule* **2025**, *9*, 101823.

Manuscript received: April 12, 2025
Revised manuscript received: June 20, 2025
Accepted manuscript online: June 23, 2025
Version of record online: July 04, 2025